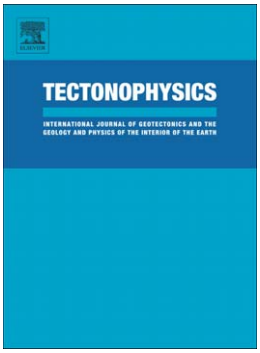

Initiation of a thrust fault revealed by analog experiments

Tatsuya Dotare, Yasuhiro Yamada, Juergen Adam, Takane Hori, Hide Sakaguchi

PII: S0040-1951(16)00003-2
DOI: doi: 10.1016/j.tecto.2015.12.023
Reference: TECTO 126889

To appear in: *Tectonophysics*

Received date: 2 June 2015
Revised date: 28 November 2015
Accepted date: 23 December 2015

Please cite this article as: Dotare, Tatsuya, Yamada, Yasuhiro, Adam, Juergen, Hori, Takane, Sakaguchi, Hide, Initiation of a thrust fault revealed by analog experiments, *Tectonophysics* (2016), doi: 10.1016/j.tecto.2015.12.023

Initiation of a thrust fault revealed by analog experiments

Tatsuya Dotare[1], Yasuhiro Yamada[12], Juergen Adam[3], Takane Hori[2], Hide Sakaguchi[2]

1. Department of Urban Management, Kyoto University, Kyoto, Japan

2. Japan Agency for Marine-Earth Science and Technology (JAMSTEC), Yokohama, Japan

3. Department of Earth Sciences, Royal Holloway University of London, Egham, UK

Corresponding author: Yasuhiro Yamada, yyamada@jamstec.go.jp

Keywords: thrust initiation, analog model, digital image correlation

Abstract

To reveal in detail the process of initiation of a thrust fault, we conducted analog experiments with dry quartz sand using a high-resolution digital image correlation technique to identify minor shear strain patterns for every 27 μm of shortening (with an absolute displacement accuracy of 0.7 μm). The experimental results identified a number of “weak shear bands” and minor uplift prior to the initiation of a thrust in cross-section view. The observations suggest that the process is closely linked to the activity of an adjacent existing thrust, and can be divided into three stages. Stage 1 is

characterized by a series of abrupt and short-lived weak shear bands at the location where the thrust will subsequently be generated. The area that will eventually be the hanging wall starts to uplift before the fault forms. The shear strain along the existing thrust decreases linearly during this stage. Stage 2 is defined by the generation of the new thrust and active displacements along it, identified by the shear strain along the thrust. The location of the new thrust may be constrained by its back-thrust, generally produced at the foot of the surface slope. The activity of the existing thrust falls to zero once the new thrust is generated, although these two events are not synchronous. Stage 3 of the thrust is characterized by a constant displacement that corresponds to the shortening applied to the model. Similar minor shear bands have been reported in the toe area of the Nankai accretionary prism, SW Japan. By comparing several transects across this subduction margin, we can classify the lateral variations in the structural geometry into the same stages of deformation identified in our experiments. Our findings may also be applied to the evaluation of fracture distributions in thrust belts during unconventional hydrocarbon exploration and production.

1. Introduction

Analog modeling has been used since the nineteenth century to evaluate how geological

structures are formed, and to understand the mechanisms controlling the geometry and kinematics of these structures (e.g., Koyi, 1997,). For many decades we have been concerned about how to measure experimental deformations quantitatively. Recently, improvements in computational resources and the resolution of digital charge coupled device (CCD) cameras have made it possible to calculate the displacement field at a high spatial resolution (Graveleau et al., 2012). Previous studies have shown that these new techniques can reveal in detail the styles of strain accumulation and distribution in analog models (e.g., Adam et al., 2005; Hoth et al., 2006a, 2007; Cruz et al., 2008; Pons and Mourgues, 2012, Yamada et al., 2014).

By applying the digital image correlation (DIC) technique to the compressional wedge model, Adam et al. (2005) reported the complex interaction of different deformation mechanisms during shear localization (initiation of the frontal thrust) as follows.

A: Underthrusting of the input layer prior to basal shear zone initiation.

B: Basal shear zone propagation and diffuse shear strain in the input layer.

C: Spontaneous strain localization in conjugate shear zones.

D: New active thrusting and a continuous frontal–basal shear zone.

Although these complex deformation stages have been reported, the DIC

technique has been used mainly for visualizing the overall deformation in a wide range of structures, for example on the scale of an accretionary wedge (Hoth et al., 2006b, 2007; Yamada et al., 2014). Few studies have focused on the process by which a new thrust is initiated; e.g., Bernard et al. (2007), who used digital image based analysis.

In this paper we aim to identify the phenomena that occur before new thrusts are initiated. Our observations focus on the frontal thrust area where the deformation is analyzed in detail using the DIC technique.

2. Methods

We used scaled 2D analog modeling experiments, with high-resolution DIC analysis, to extract the spatial and temporal distributions of the minor deformation (shear strain in this study) associated with the initiation of the frontal thrust. Scaled analog modeling has been widely used to represent the geometry and process of deformation of geological structures (see the following reviews: Koyi, 1997; Buiter, 2012; Graveleau et al., 2012). Previous studies have investigated the mechanical properties of granular materials and their scaling properties (Krantz, 1991; Schellart, 2000) and their non-linear strain-dependent mechanical behavior (Lohrmann et al., 2003; Adam et al., 2005; Panien et al., 2006). Lohrmann (2003) argued that granular materials obey

elastic–frictional plastic deformation with pre-failure strain hardening and post-failure strain softening until a dynamically constant shear load is reached. This is similar to the nonlinear deformational behavior of brittle rocks, suggesting that granular material (especially dry quartz sand) can fulfil the conditions of dynamic similarity and accurately simulate crustal tectonic processes. To model the process of initiation of the thrust fault, we used a simple shortening experiment with dry quartz sand.

2.1. Experimental setup

The experimental setup consisted of a box of 25 × 90 × 30 cm (height, length, width) in dimensions equipped with a moving wall, a transparent side-glass, a plastic Teflon base, and digital cameras (Figure 1). As suggested by Schreurs et al (2006), the sidewall has frictional effects, and the shape of thrust fault is curved by the side-wall friction. To minimize this effect, the glass surfaces were coated with a low friction agent.

We used low cohesion quartz sand (Toyoura sand) as the granular material, and its thickness was 4 cm. Toyoura sand is a beach sand, popular among Japanese civil engineers for physical tests. To minimize potential pre-defined weak planes and any heterogeneity in the initial state of the experimental material, we used a custom-made sand distributor, which automatically produces a homogeneous layer of sand. Marker

layers to visualize the deformation were not inserted, but we mixed sand that had been dyed in three different colors to emphasize the granular pattern for digital image correlation. The properties of the mixed sand and the Teflon base were tested using a series of ring shear tests under normal loads comparable to experimental conditions. The material tests confirmed that the Toyoura sand shows a nonlinear stress-strain relationship with elastic–frictional plastic deformation behavior. Shear zone formation is accompanied by a characteristic cycle of material compaction and decompaction caused by distributed strain during pre-failure strain hardening followed by shear failure at peak strength and shear localization with post-failure strain softening during ongoing deformation. As consequence of the decompaction and strain softening during shear localization, weaker pre-existing shear zones are characterized by lower strength and decreased frictional coefficients. All relevant material parameters for the experiment materials are summarized in Table 1.

The strain softening of the sand material and pre-existing shear zones describes the drop in stress and strength during shear localization (see table 1). Strain softening for the Toyoura sand varies from 23.6 % for undeformed material to 14.6% for reactivation of internal shear zones. Strain softening along the basal interface of Toyoura sand to the Teflon base varies from 24.3 % for basal shear zone localization

(undeformed sand material on Teflon base) to 10.1% % for basal shear zone reactivation (deformed sand material on Teflon base).

The sand layer was deformed by the moving wall, activated by an electrically controlled motor at a constant speed of 0.33 mm/minute (2.0 cm/hour). During the experiments, the deformation was recorded through the side-glass by digital cameras until the second thrust showed active deformation. Figure 2 shows an example of the final phase of the experiments, together with the location of the area of analysis and the first (existing) and the second (new) thrusts. Two cameras were used to cover the areas of interest (with 1.0 cm overlap) to maintain the required high resolution (Figure 1).

2.2. DIC analysis with LES decomposition

DIC is a technique used to extract the displacement field from pairs of time-lapsed digital images by matching the patterns of pixel color values. In other words, the resolution of DIC analysis is based on the resolution of digital images and the size of the recorded area. To extract information on a small deformation (strain), we used two 16.0 megapixel digital cameras, each with a pixel size of 20 μm in our configuration, and recording every 5 seconds (i.e., for 27.5 μm of wall displacement). This analysis not only extracts the velocity field in the model but also the strain value from the velocity

pattern. To minimize the calculation errors derived from the stitching effect of the two images, we first calculated the strain value separately, then connected the two calculated results (Figure 3). Since we set the interrogation window (unit for pattern matching) size at 32 × 32 pixels with 50% overlap, the theoretical accuracy of displacement was 0.025 pixels (0.5 μm) (LaVision GmbH, 2012). This configuration of data acquisition made it possible for us to detect a finer detail of deformation than achieved previously in analog modeling (see Table 2). We used commercial software StrainMaster of LaVision GmbH.

Since the deformation values obtained are extremely small, it is difficult to distinguish the small strain distribution pattern from the "artificial strain" due to the velocity gradient, because of errors caused by the random noise in the CCD acquisition patterns. To minimize this error and to clarify the very small deformation in the model, we applied the non-linear large eddy simulation (LES) decomposition filter (Adrian et al., 2000). There are a number of decomposition filters for detecting small-scale vortices in flow dynamics, and LES decomposition is the best method (Adrian et al., 2000; LaVision, 2012). In our study, given the quasi-static setting of the model and the short-term correlation interval (per 27.5 μm of wall displacement), the turbulence or small-scale vortices in our results are unexpected. Therefore, we applied this filter to

remove most of the artificial small-scale vortices, after which we extracted the distribution of strain (Figure 4a).

Although the artificial strain distribution is reduced by LES decomposition, an inhomogeneous strain distribution persists (Figure 4b). It has been reported that lens distortion can hamper the strain identification process (Lava et al., 2013). From Figure 4b, we can identify the differences in the strain distribution between the center and the outer sides of the images. Therefore, in this paper we focus on the qualitative transitional pattern rather than the absolute value of the derived strain.

3. Experimental results

3.1. Overall deformation pattern

Based on the time-series activity of two thrusts, one existing and one new, that can be identified from incremental shear strain patterns (Figure 5), we divide the initiation process of the frontal thrust into three stages. We have observed the detailed characteristics of the temporal strain patterns at each stage of deformation in the shear strain distributions calculated for every 27 μm of wall displacement (Figure 6).

Stage 0 (Pre-stage 1)

While the existing thrust maintains a constant slip rate (Figure 5a), we do not identify any shear-strain pattern in the foreland of the thrust (Figure 6a). The area that will be the hanging wall shows no motion (Figure 5b).

Stage 1

Shear strain along the existing thrust decreases linearly with convergence, and we identify a series of abrupt and short-lived subtle shear strains at the location of the new thrust. These "weak shear bands" are sub-parallel to each other and dip to the right-hand side, and the location of each band changes systematically and rapidly (Figure 6b). In other words, these bands do not stay in the same location for more than three consecutive increments (81 μm of wall displacement). We observe the activity of the shear bands throughout this stage. The area that will be the hanging wall of the new thrust starts to uplift at a constant rate (Figure 5b), even prior to the formation of the thrust fault surface.

Stage 2

The weak shear bands start to localize at a specific location to form the new thrust

(Figure 6c), and the shear strain along this thrust starts to increase significantly (Figure 5a). At the same time, the hanging wall of the thrust is uplifted significantly, but the rate (for every 18 μm) is not constant, and it exhibits a peak in the middle of this stage (Figure 5b). Once the strain localization starts, the rapidly moving weak shear bands can no longer be observed. The shear strain along the existing thrust decreases significantly and falls to a background level (Figure 6c), but this was not synchronous with the emergence of the new thrust (Figure 5a).

Stage 3

The shear-strain along the new thrust reached a value similar to that of the existing thrust in stage 0, and subsequently the shear-strain value remains constant within a narrow shear band (Figures 5a and 6d). The uplift of the hanging wall continues during this stage (Figure 5b).

3.2. Details of temporal strain accumulation in stage 1

The experimental results show that the deformation pattern is characterized by weak shear bands during stage 1. To clarify the location of these weak shear bands, which do not remain in the same location, we calculated the distributions of incremental and

cumulative strains and compared their patterns. Figure 7 shows an example of the incremental and cumulative strains calculated for a shortening between 15.50 mm and 15.75 mm. The cumulative strains, calculated using a Lagrangian summation of the incremental displacement field, show that the location of the weak shear bands is not random but the shear bands are generated at low strain regions between the bands. As the deformation proceeds, the shear strain is widely distributed without forming any concentrations of strain, except for a shear zone dipping to the opposite (i.e. back-thrust) at the foot of the surface slope.

4. Discussion

4.1. Conceptual model of thrust fault initiation

Based on the observations described above, we propose the following conceptual model for initiation of a thrust fault (Figure 8).

Stage 1: This is the deformation propagation stage (cf. Figures 6–8), characterized by ephemeral minor “weak shear bands” in front of an existing frontal thrust that is decreasing in activity. This stage may correspond to the “diffuse shear strain” distribution of Adam et al. (2005). However, our detailed observations in terms of

temporal and spatial resolution revealed that this "diffusive" deformation is the sum of the activity of numerous short-lived weak shear bands (Figure 7). These features are compatible with the previously reported patterns of shear banding in sand under plane strain compression where the shear strain is initiated along a number of parallel and conjugate planes prior to the peak stress (Rechenmacher, 2006). Therefore, during this stage, a number of minor thrust faults in the foreland may have been associated with the propagation of shortening deformation. The accommodation of the shortening by the minor shear bands may also be responsible for the uplift (cf. Figure 5b) in the area of the future hanging wall.

Stage 2: This is the stage of strain localization and thrust initiation (cf. Figures 6–8). The shear strain starts to localize, and the location of the new frontal thrust is determined at one of the minor weak shear bands that form during the process of localization. Other weak shear bands become inactive, and the movements along the existing thrust abruptly cease. This process corresponds to what has previously been noted as the "strain localization" or "thrust initiation" stages that are associated with the time when the materials reach peak strength (Lohrmann et al., 2003; Adam et al., 2005). The rate of uplift of the hanging wall (Figure 5b) also shows a pattern similar to this

peak strength behavior.

The location of the new frontal thrust seems to be constrained by its associated back-thrust whose location is generally at the foot of the surface slope (Figures 6-8). Since this surface topography is induced by the displacement of the previous thrust, the location of the new thrust is determined by the location of the previous thrust and the thickness above the detachment surface. Ruh et al (2012) reported a similar finding after their numerical simulations and also state that the dip of the new thrust is different from the ones within the wedge. We see the same thrust dip characteristics in our analog model.

Stage 3: This is the active frontal thrust stage (cf. Figures 6–8), at which time the newly initiated thrust is the only active fault showing a constant rate of strain. The stage corresponds to the “after failure and stable sliding phase” of shear tests in granular materials (Lohrmann et al., 2003). During stage 3, the strain is released only by the new frontal thrust, and the total shear strain along the new thrust become significant.

4.2. Comparisons with natural examples

Since our experiments focused on the initiation process of a frontal thrust, we examined

the proto-thrust zones (PTZ) of two subduction margins for comparison.

Cascadia

The PTZ of the Cascadia accretionary margin, offshore from the northwestern coast of North America, contains a number of sub-parallel proto-thrusts with small displacements, and several of them show low-amplitude negative polarity reflection in the seismic dataset (Moore et al., 1995). This phenomenon suggests fluids may have migrated along these faults from depth.

During stage 1 of our model (Figure 8), "weak shear bands" rapidly change their locations, and they may develop numerous sub-parallel active proto-thrusts that may act as fluid migration paths, following the idea presented by Yamada et al (2014). On the other hand, once the frontal thrust has been initiated, strain is mainly accommodated by the new thrust, and proto-thrusts are no longer generated. During stages 2 and 3, the fluids migrate mainly along the new active frontal thrust, and the proto-thrusts may not show any clear seismic anomaly of negative polarity. According to above discussion, we can infer that the sub parallel seismic anomaly at the toe of Cascadia margin suggest they are under Stage 1.

Nankai

At the toe of the Nankai accretionary prism in SW Japan, there is a proto-thrust zone (PTZ) where the Philippine Sea plate is being subducted beneath the southwest Japan arc (Eurasian plate), and where sediment is actively accreting (Moore et al., 2001). According to previous studies (e.g., Morgan et al., 1995), the structural domain varies between two parallel transects of the Nankai prism off Cape Ashizuri and Cape Muroto, which are 130 km apart. The toe of the Ashizuri transect has a well-developed PTZ containing numerous sub-parallel dipping discontinuities, whereas the Muroto transect has only a narrow PTZ and few discontinuities. Moore et al. (2001) suggested that these variations might be the result of differences in mechanical properties and/or pore pressures.

Based on the stages of deformation we proposed from our experiments (Figure 8), together with information from the Cascadia margin, the interpretation of the Muroto–Ashizuri transects by Moore et al. (2001) can be revised. The sub-parallel discontinuities in the Ashizuri PTZ may correspond to the "weak shear bands" observed in our experiments (Figure 7b), and the along-strike variation between the two transects may correspond to different stages in the initiation of the frontal thrust rather than changes in mechanical properties. Since the surface topography of the Muroto transect

PTZ indicates more deformation than in the Ashizuri transect, the Muroto PTZ may be at a later stage of development. In other words, the Ashizuri PTZ may be in stage 1 of its development, with numerous active proto-thrusts acting as the migration paths for fluids, and producing a seismic discontinuity (cf. Cascadia margin). On the other hand, the Muroto PTZ may be at stage 2 or stage 3, and only the one active thrust is seismically active due to the fluid flow being concentrated along that fault. By analogy with our model results, the Muroto PTZ might have been wider in the past with more proto-thrusts, but these minor features have now disappeared and can no longer be detected since their fault displacements are too small to be detected in the seismic data. This proposition is consistent with the existence of deformation bands with reverse displacements in the core samples recovered from the ODP 1174 site, which was drilled through the Muroto proto-thrust (Ujiie et al., 2004).

4.3. Implications for hydrocarbon exploration/production

Shale gas and oil have been highlighted in recent years as unconventional hydrocarbon resources, particularly in the USA (Montgomery et al., 2005; Bowker, 2007), and the detection of “sweet spots” (highly productive targets) has been the key issue. Since shale gas reservoirs are of extremely low permeability, natural fractures play a major

role in every stage of the accumulation, preservation, and production of the hydrocarbons (Curtis, 2002; Slatt and O'Brien, 2011; Ding et al., 2012, 2013). The detection of sub-seismic natural fracture systems using geophysical exploration techniques remains challenging, and the model proposed in this study may provide insights into a potential approach for thrust belts. For example, in the case that the deformation stage of a thrust belt, as identified from seismic and topographic/bathymetric datasets, can be considered to be in stage 1 of the model presented in this paper, we can expect relatively new (possibly permeable) minor fracture systems in the foreland of the frontal thrust.

4.4. Implications for bridging the gap between seismic and well data

Seismic data provide information on large geological structures over tens of kilometers in length, whereas geophysical logging and core data can be used to characterize small structures (mm to a few meters) at the wells (Gauthier and Lake, 1993). Thus, a significant scale gap exists between these subsurface data sources (Strijker et al., 2012), and the combined use of these data requires an in-depth knowledge of the methods that underlie the datasets (Yamada et al., 2011). Our conceptual model may help to bridging these scale gaps by providing a greater understanding of the geological process in detail.

5. Conclusions

With the use of high-resolution digital image correlation analysis, we have conducted detailed analog sandbox modeling with a focus on the initiation of frontal thrusts. In our experiments, "weak shear bands" and strain concentration are identified in the area where the new thrust is later to be initiated. We divide initiation process of a thrust into three stages:

Stage 1: Propagation of the deformation to the undeformed foreland of existing thrust.

Stage 2: Strain localization and initiation of a new thrust.

Stage 3: Active displacement upon the thrust.

By comparing our experimental results with the geometry of the Nankai accretionary prism, we infer that the along-strike variations in structural geometry observed in the toe area may be due to these areas being at different stages of deformation.

Since our experimental configuration is one of simple shortening, our conceptual model can be applied to any fold-and-thrust belt. By taking into account the deformation stage of the target structure, we can estimate the potential presence of sub-seismic scale fractures or minor faults, which may be significant in terms of

assessing the productivity of a hydrocarbon reservoir.

Acknowledgments

Funding for this research was provided by Grants-in-Aid for Scientific Research (KAKENHI: 213101115, 23340134 and 24540489) and for Scientific Research on Innovative Areas (21107002) from Japan Society for the Promotion of Science (JSPS). We acknowledge the guest editors, Karen Leever and Onno Oncken, and two reviewers, Jonas Ruh and Michele Cooke, for their constructive comments.

Figure 1. Experimental setup. The experimental material (dry sand) is set on a Teflon base. The left wall is fixed and the right wall is displaced at a constant speed by an electrical motor. Two cameras are used to record the 2D cross-sectional deformation around the thrust initiation area through the transparent glass-sidewall.

Figure 2. Example of the final state of an experiment. The locations of the existing and new frontal thrusts are indicated by dashed and solid lines, respectively. The rectangular box shows the area of recording, focusing on the area in which the new frontal thrust initiates.

Figure 3. Analytical procedure used in this study. (a) Digital picture taken by two (left and right) cameras, (b) digital image analysis undertaken for the two pictures separately, and (c) connection of the two results to determine the spatial distribution of maximum shear strain around the area of initiation of the new (2nd) frontal thrust.

Figure 4. Effects of LES decomposition filter. (a) Noise reduction by this method. These patterns are obtained by using images of the undeformed foreland area after 1.0 mm of shortening. The artificial shear strain due to the minor vortices (artifacts) widely distributed in the initial calculation (left) can be significantly reduced by applying the LES decomposition (right). The arrows are 400 times exaggerated. (b) Remaining pattern of inhomogeneous strain distribution (background noise) after LES decomposition. The distribution of artificial background noise across the images (above) are for an average of 5 time-lapsed analyses, and they show gradual increases towards the edges.

Figure 5. Detailed time-series analysis of the frontal thrust. (a) Incremental maximum shear strain along the two thrusts, obtained by DIC analysis. The boxes (ca. 64 mm^2

each) correspond to the sampling locations where the mean strains were calculated. (b) Amount of uplift of the hanging wall, showing the location used for the calculations (indicated by a box).

Figure 6. Detailed temporal evolution of the shear strain distribution for each 27 μm of wall displacement, representing the characteristics of the three stages of thrust initiation. The timings for these strain distributions are indicated in Figure 5. (a) Before stage 1, only the existing thrust is active. (b) In stage 1, the weak shear bands (marked by arrows) are active in the foreland area of the existing thrust while the thrust is still active. (c) In stage 2, the new thrust initiates and the activity of the existing thrust (marked by the arrow) decreases. (d) In stage 3, only the new thrust is active.

Figure 7. Incremental (left) and cumulative (right) strain distributions in stage 1, based on the time-series data for wall displacement of 15.50 to 15.75 mm. It is clear that the "diffusive" strain in front of the previous frontal thrust is the sum of the minor shear strain generated by a number of short-lived weak shear bands.

Figure 8. Conceptual model, in three stages, for the initiation of a frontal thrust:

propagation of deformation (stage 1), strain localization and thrust initiation (stage 2), and active displacement upon the frontal thrust (stage 3). See text for more detail.

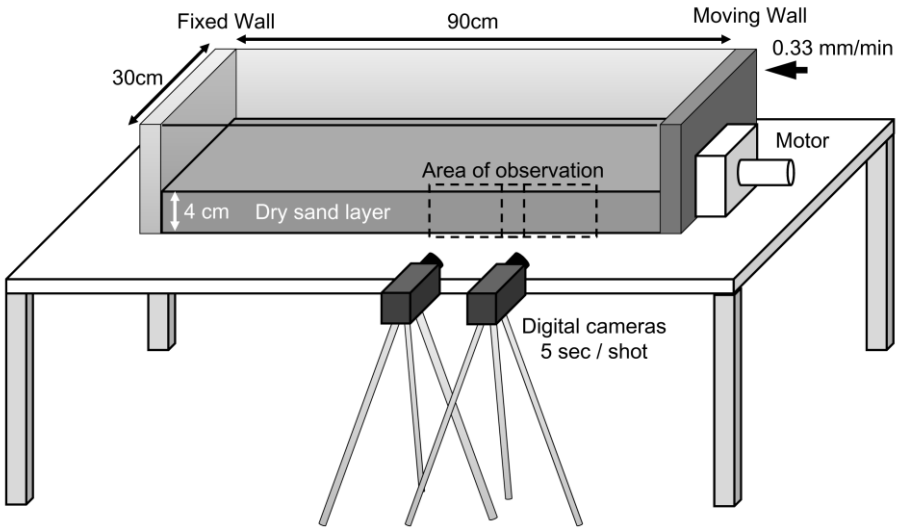

FIG. 1

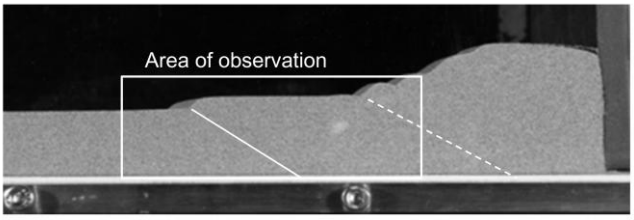

Fig. 2

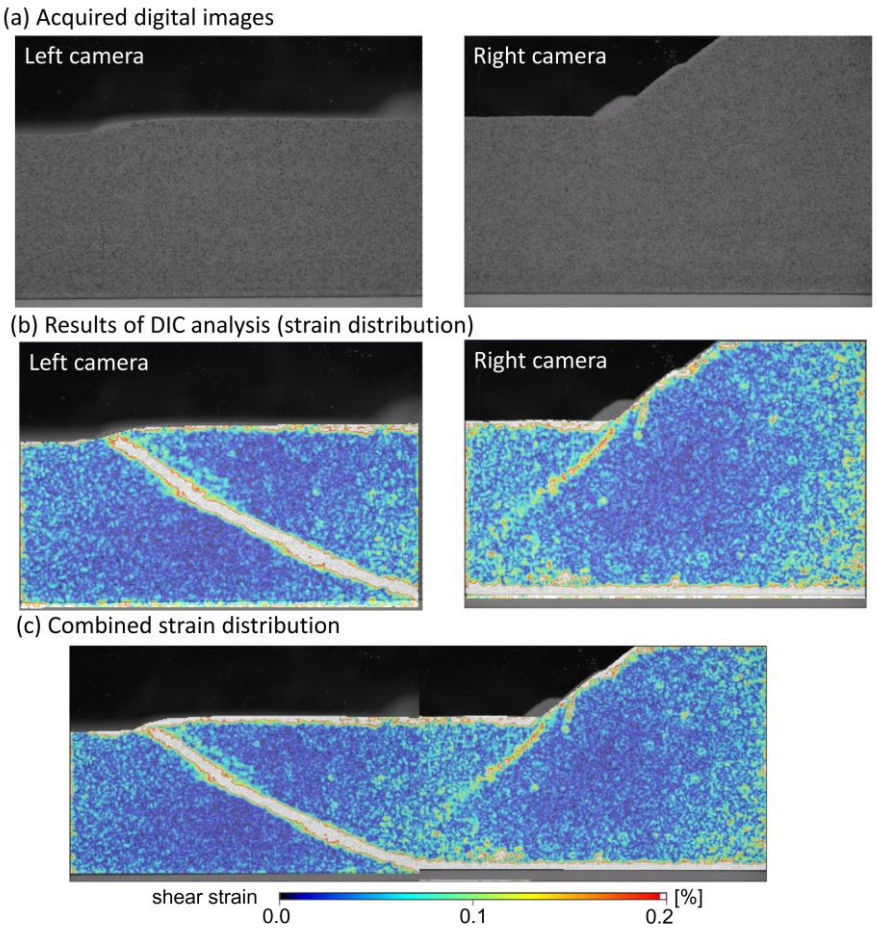

Fig. 3

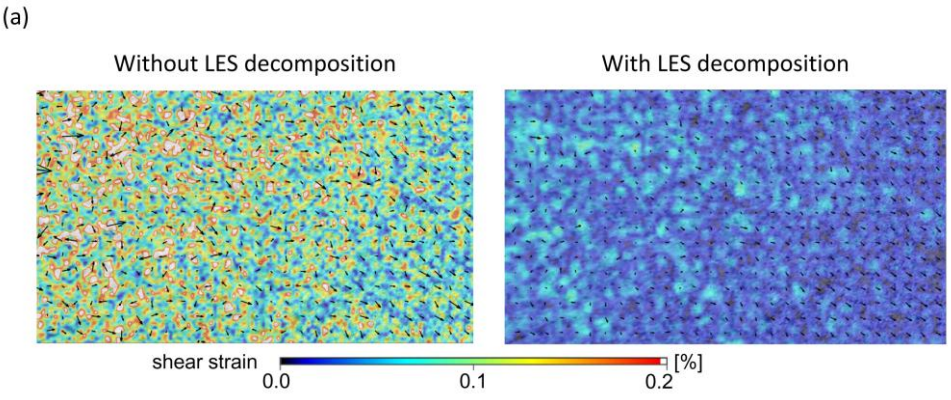

Fig. 4a

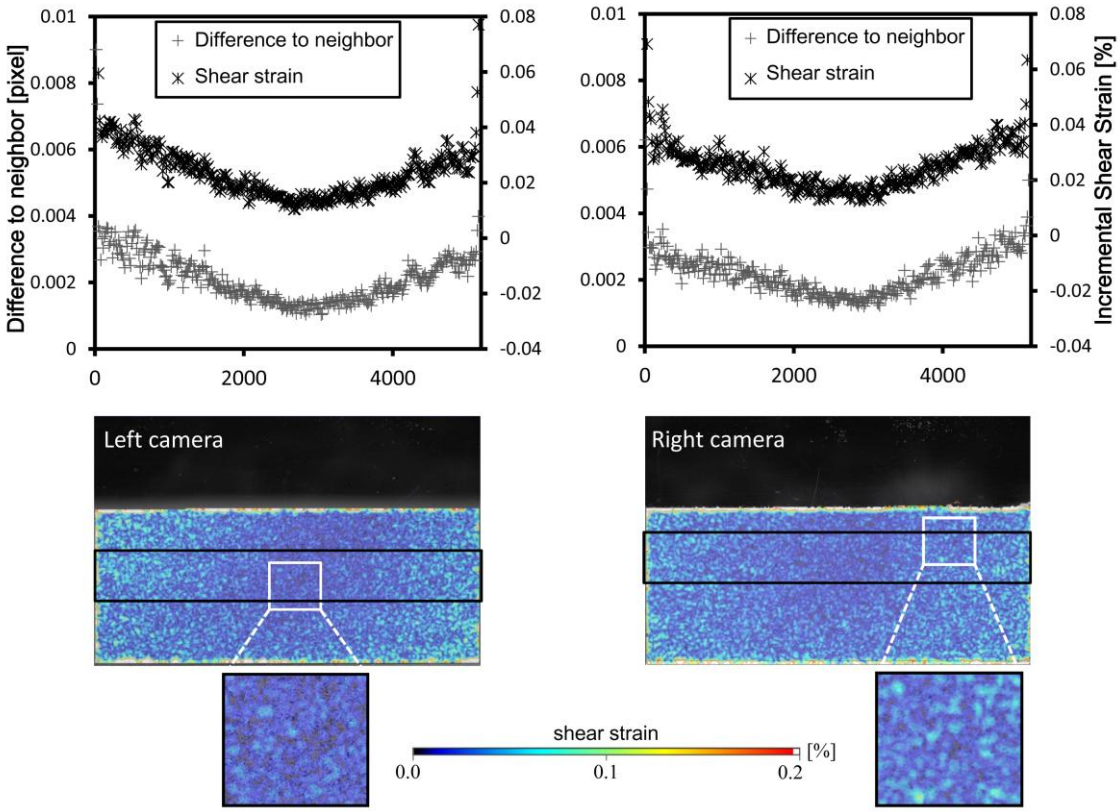

Fig. 4b

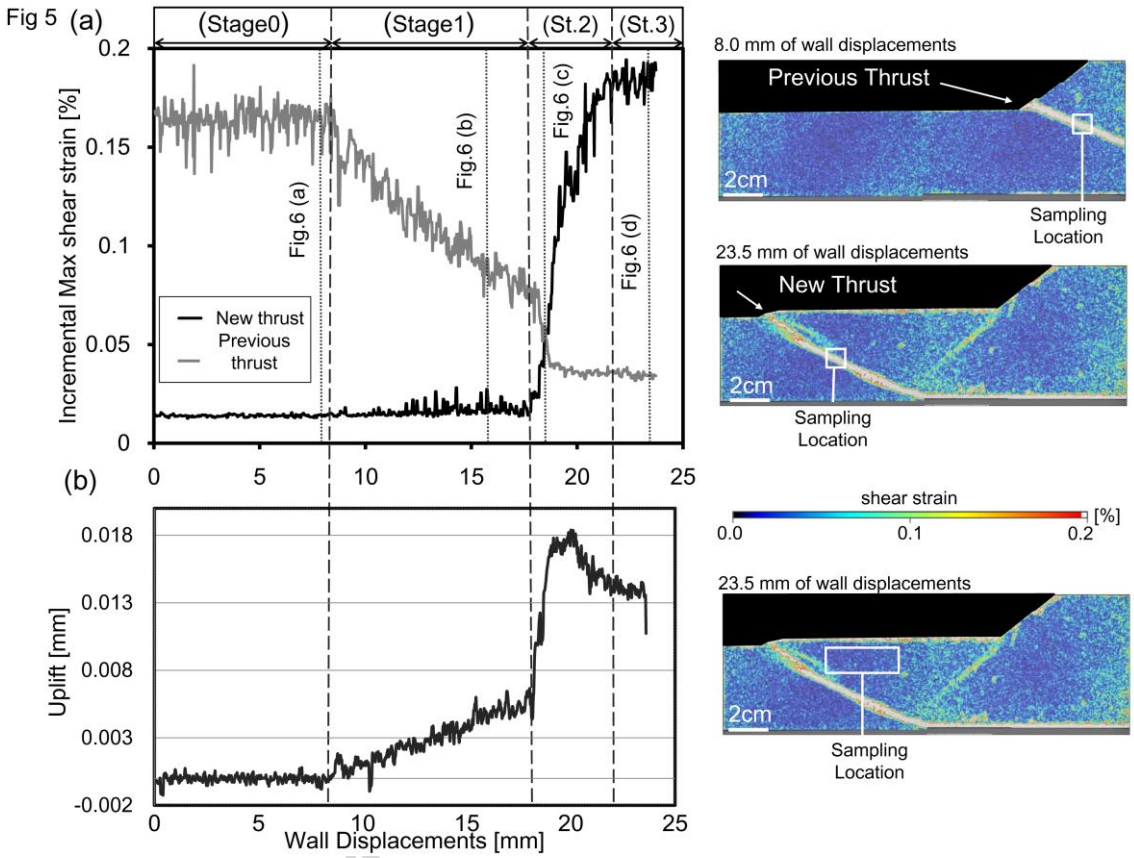

Fig. 5

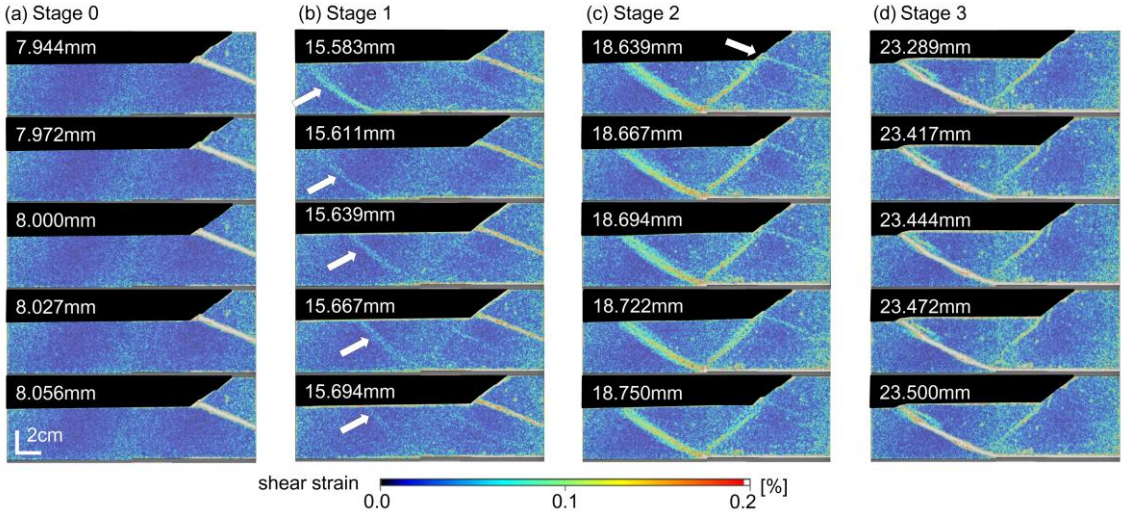

Fig. 6

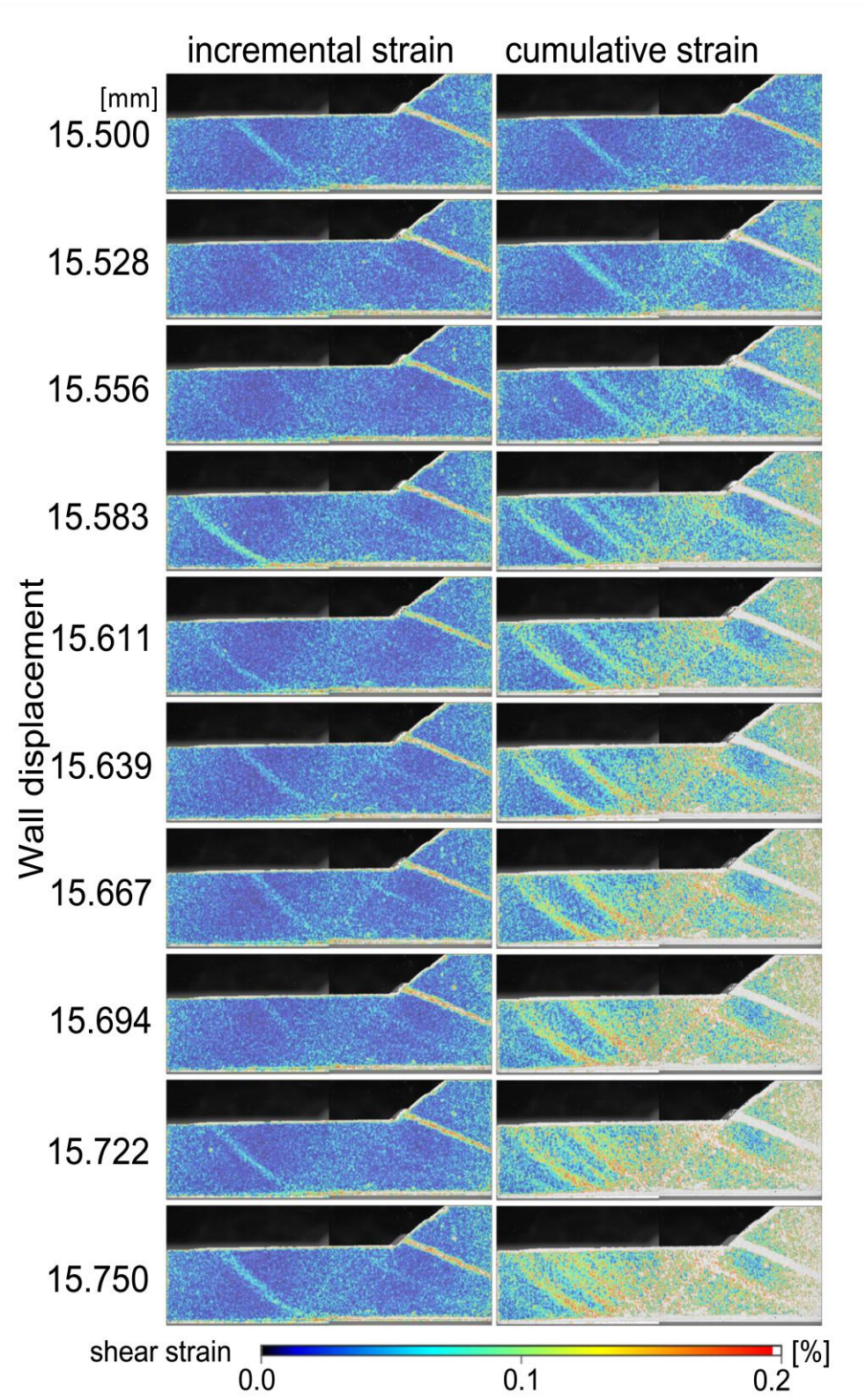

Fig. 7

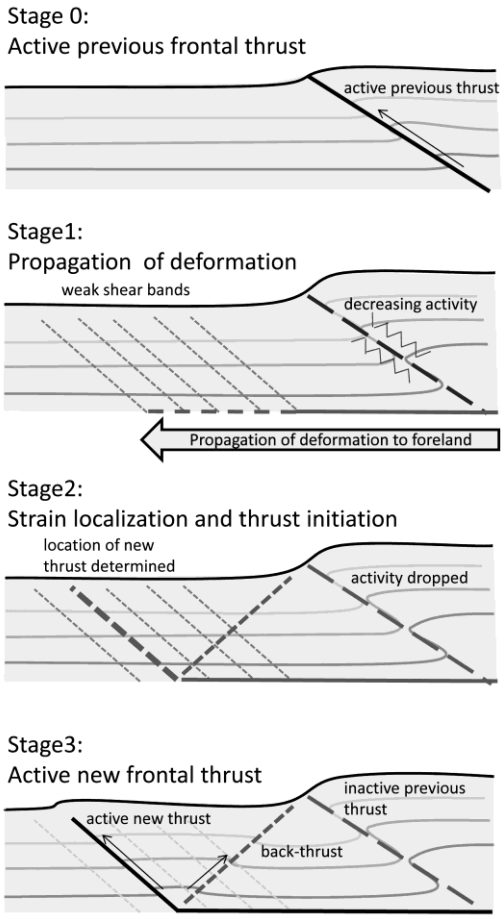

Fig. 8

Table 1. Physical properties of analog materials used in the sandbox experiments. We used a ring shear tester (RST-01.pc) to measure the internal coefficient of friction and the cohesion C. The suffixes “peak”, “static”, and “dynamic” indicate the property of the undeformed material, previously deformed material, and active shear zones, respectively.

material		Toyoura sand internal	Toyoura sand on basal shear zone
grain size (μm)		106-300*1	—
preparation		Sifted	relative to sifted sand
density (g/cm3)		1.602	—
μ_{peak}		0.728±0.008	0.271±0.013
C_{peak} (Pa)		157±13	—
μ_{static}		0.675±0.004	0.240±0.011
C_{static} (Pa)		127±7	95±20
$\mu_{dynamic}$		0.589±0.003	0.218±0.013
$C_{dynamic}$ (Pa)		105±5	78±17
strain softening (%)	undeformed material	0.236-23.6*2	0.243-24.3*4
	shear zone reactivation	0.146-14.6*3	0.101-10.1*5

*1 Yamada et al., 2010

*2 Ratio of the friction coefficients: [peak strength - dynamic strength] / dynamic strength in percent. For Toyoura sand strain softening: 0.236 ~ 23.6%.

*3 Ratio of the friction coefficients [static strength - dynamic strength] / dynamic strength in percent. For Toyoura sand strain softening for fault reactivation: 0.146 ~ 14.6%.

*4 Ratio of the friction coefficients: [peak strength - dynamic strength] / dynamic strength in percent. For Toyoura sand on Teflon strain softening: 0.243 ~ 24.3%.

*5 Ratio of the friction coefficients: [static strength - dynamic strength] / dynamic strength in percent. For Toyoura sand on Teflon strain softening: 0.101 ~ 10.1%.

Table 2. Comparisons of the temporal resolutions and displacement accuracies between this study and previous studies.

method	reference	temporal resolution (mm of shortening)	absolute displacement accuracy
DIC	Adam et al., 2005	22	0.05-0.5mm
	Hoth et al., 2006b, 2007, 2008	7.5	0.5mm
	Cruz et al., 2008, 2010	60	0.015mm
	Pons and Mourgues, 2012	0.75	0.1-0.5mm
	Yamada et al., 2014	0.25	2.43μm
	this study	0.027	0.5 μm
optical flow	Bernard et al., 2007	0.235	5%

Graphical Abstract

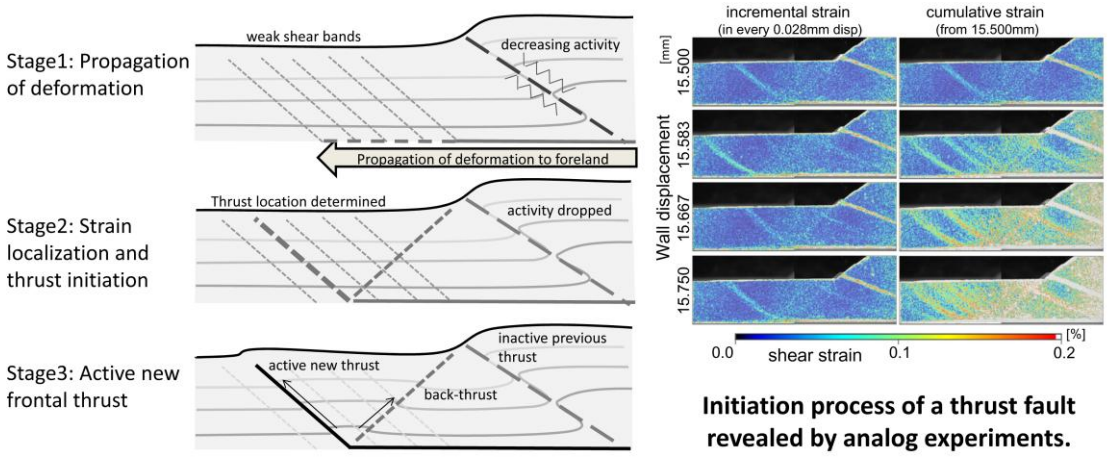

Highlights

- Thrust initiation process can be divided into three stages.
- Many abrupt and short-lived weak shear bands are produced before thrust initiation.
- Hanging wall starts to uplift before new thrust fault forms.
- Location of new thrust is determined by its back-thrust.
- Lateral structural variations can be due to different stages of thrust initiation.

REFERENCES

Adam, J., Urai, J.L., Wieneke, B., Oncken, O., Pfeiffer, K., Kukowski, N., Lohrmann, J., Hoth, S., van der Zee, W., Schmatz, J., 2005. Shear localisation and strain distribution during tectonic faulting—new insights from granular-flow experiments and high-resolution optical image correlation techniques. Journal of Structural Geolology 27, 283–301. doi:10.1016/j.jsg.2004.08.008

Adrian, R.J., Christensen, K.T., Liu, Z.-C., 2000. Analysis and interpretation of instantaneous turbulent velocity fields. Exp. Fluids 29, 275–290. doi:10.1007/s003489900087

Bernard, S., Avouac, J.-P., Dominguez, S., Simoes, M., 2007. Kinematics of fault-related folding derived from a sandbox experiment. Journal of Geophysical Research 112, B03S12. doi:10.1029/2005JB004149

Bowker, K.A., 2007. Barnett Shale gas production, Fort Worth Basin: Issues and discussion. American Association of Petroleum Geologists Bulletin 91, 523–533. doi:10.1306/06190606018

Buiter, S.J.H., 2012. A review of brittle compressional wedge models. Tectonophysics 530-531, 1–17. doi:10.1016/j.tecto.2011.12.018

Cruz, L., Malinski, J., Wilson, a., Take, W. a., Hilley, G., 2010. Erosional control of the kinematics and geometry of fold-and-thrust belts imaged in a physical and numerical sandbox. Journal of Geophysical Research 115, B09404. doi:10.1029/2010JB007472

Cruz, L., Teyssier, C., Perg, L., Take, A., Fayon, A., 2008. Deformation, exhumation, and topography of experimental doubly-vergent orogenic wedges subjected to asymmetric erosion. Journal of Structural Geolology 30, 98–115. doi:10.1016/j.jsg.2007.10.003

Curtis, J.B., 2002. Fractured shale-gas systems. American Association of Petroleum Geologists Bulletin 86, 1921–1938. doi:10.1306/61EEDDBE-173E-11D7-8645000102C1865D

Ding, W., Li, C., Li, C., Xu, C., Jiu, K., Zeng, W., Wu, L., 2012. Fracture development in shale and its relationship to gas accumulation. Geoscience Frontier 3, 97–105. doi:10.1016/j.gsf.2011.10.001

Ding, W., Zhu, D., Cai, J., Gong, M., Chen, F., 2013. Analysis of the developmental characteristics and major regulating factors of fractures in marine–continental transitional shale-gas reservoirs: A case study of the Carboniferous–Permian strata in the southeastern Ordos Basin, central China. Marine and Petroleum Geology 45, 121–133. doi:10.1016/j.marpetgeo.2013.04.022

Gauthier, B.D.M., Lake, S.D., 1993. Probabilistic Modeling of Faults Below the Limit of Seismic Resolution in Pelican Field, North Sea, Offshore United Kingdom. American Association of Petroleum Geologists Bulletin 77, 761–777.

Graveleau, F., Malavieille, J., Dominguez, S., 2012. Experimental modelling of orogenic wedges: A review. Tectonophysics 538-540, 1–66. doi:10.1016/j.tecto.2012.01.027

Heffernan, a. S., Moore, J.C., Bangs, N.L., Moore, G.F., Shipley, T.H., 2004. Initial Deformation in a Subduction Thrust System: Polygonal Normal Faulting in the Incoming Sedimentary Sequence of the Nankai Subduction Zone, Southwestern Japan. Geological Society London Memoir 29, 143–148. doi:10.1144/GSL.MEM.2004.029.01.14

Hoth, S., Adam, J., Kukowski, N., Oncken, O., 2006b. Influence of erosion on

the kinematics of bivergent orogens: Results from scaled sandbox simulations. Geological Society of America Special Paper 398, 201–225. doi:10.1130/2006.2398(12)

Hoth, S., Hoffmann-Rothe, A., Kukowski, N., 2007. Frontal accretion: An internal clock for bivergent wedge deformation and surface uplift. Journal of Geophysical Research 112, B06408. doi:10.1029/2006JB004357

Hoth, S., Kukowski, N., Oncken, O., 2008. Distant effects in bivergent orogenic belts — How retro-wedge erosion triggers resource formation in pro-foreland basins. Earth and Planetary Science Letters 273, 28–37. doi:10.1016/j.epsl.2008.05.033

Koyi, H., 1997. Analogue modelling: from a qualitative to a quantitative technique — A historical outline. Journal of Petroleum Geology 20, 223–238. doi:10.1111/j.1747-5457.1997.tb00774.x

Lava, P., Van Paepegem, W., Coppieters, S., De Baere, I., Wang, Y., Debruyne, D., 2013. Impact of lens distortions on strain measurements obtained with 2D digital image correlation. Optical Lasers Engineering 51, 576–584. doi:10.1016/j.optlaseng.2012.12.009

LaVision, 2012. Product-Manual for Davis8.0 StrainMaster.

Lohrmann, J., Kukowski, N., Adam, J., Oncken, O., 2003. The impact of analogue material properties on the geometry, kinematics, and dynamics of convergent sand wedges. Journal of Structural Geology 25, 1691–1711. doi:10.1016/S0191-8141(03)00005-1

Montgomery, S.L., Jarvie, D.M., Bowker, K.A., Pollastro, R.M., 2005. Mississippian Barnett Shale, Fort Worth basin, north-central Texas: Gas-shale play with multi–trillion cubic foot potential. American Association of Petroleum Geologists Bulletin Bull. 89, 155–175. doi:10.1306/09170404042

Moore, G.F., Taira, A., Klaus, A., Becker, L., Boeckel, B., Cragg, B.A., Dean, A., Fergusson, C.L., Henry, P., Hirano, S., Hisamitsu, T., Hunze, S., Kastner, M., Maltman, A.J., Morgan, J.K., Murakami, Y., Saffer, D.M., Sánchez-Gómez, M., Screaton, E.J., Smith, D.C., Spivack, A.J., Steurer, J., Tobin, H.J., Ujiie, K., Underwood, M.B., Wilson, M., 2001. New insights into deformation and fluid flow processes in the Nankai Trough accretionary prism: Results of Ocean Drilling Program Leg 190. Geochemistry, Geophysics, Geosystems 2, doi:10.1029/2001GC000166

Moore, J.C., Moore, G.F., Cochrane, G.R., Tobin, H.J., 1995. Negative-polarity seismic reflections along faults of the Oregon accretionary prism: Indicators of overpressuring. Journal of Geophysical Research 100, 12895–12906. doi:10.1029/94JB02049

Morgan, J.K., Karig, D.E., Maniatty, A., 1994. The estimation of diffuse strains in the toe of the western Nankai accretionary prism: A kinematic solution. Journal of Geophysical Research 99, 7019–7032. doi:10.1029/93JB03367

Morley, C.K., King, R., Hillis, R., Tingay, M., Backe, G., 2011. Deepwater fold and thrust belt classification, tectonics, structure and hydrocarbon prospectivity: A review. Earth-Science Rev. 104, 41–91. doi:10.1016/j.earscirev.2010.09.010

Pons, A., Mourgues, R., 2012. Deformation and stability of over-pressured wedges: Insight from sandbox models. Journal of Geophysical Research 117, B09404. doi:10.1029/2012JB009379

Rechenmacher, A.L., 2006. Grain-scale processes governing shear band initiation and evolution in sands. Journal Mechanics Physics Solids 54, 22–45. doi:10.1016/j.jmps.2005.08.009

Schreurs, G., Buiter, S.J.H., Corti, G., Costa, E., Hoth, S., Koyi, H., Kukowski, N., Lohrmann, J., Schlische, R., Withjack, M.O., Boutelier, D., Cavozzi, C., Cruden, A., Daniel, J-M., DelVentisette, C., Brady, J.E., Hoffmann-Rothe, A., Mengus, J-M., Montanari, D., Nilforoushan, F., Ravaglia, A. & Yamada, Y., 2006. Analogue benchmarks of shortening and extension experiments. In: Buiter, S. and Scherurs, G. (Eds.), Numerical and

Analogue Modelling of Crustal-Scale Processes, Geological Society Special Publication 253. 1-27. doi: 10.1144/GSL.SP.2006.253.01.01

Slatt, R.M., O'Brien, N.R., 2011. Pore types in the Barnett and Woodford gas shales: Contribution to understanding gas storage and migration pathways in fine-grained rocks. American Association of Petroleum Geologists Bulletin 95, 2017–2030. doi:10.1306/03301110145

Strijker, G., Bertotti, G., Luthi, S.M., 2012. Multi-scale fracture network analysis from an outcrop analogue: A case study from the Cambro-Ordovician clastic succession in Petra, Jordan. Mar. Pet. Geol. 38, 104–116. doi:10.1016/j.marpetgeo.2012.07.003

Ujiie, K., Maltman, A.J., Sánchez-Gómez, M., 2004. Origin of deformation bands in argillaceous sediments at the toe of the Nankai accretionary prism, southwest Japan. Journal of Structural Geology 26, 221–231. doi:10.1016/j.jsg.2003.06.001

Yamada, Y., Baba, K., Miyakawa, A., Matsuoka, T., 2014. Granular experiments of thrust wedges: Insights relevant to methane hydrate exploration at the Nankai accretionary prism. Marine and Petroleum Geology 51, 34–48. doi:10.1016/j.marpetgeo.2013.11.008

Yamada, Y., McNeill, L., Moore, J.C., Nakamura, Y., 2011. Structural styles

across the Nankai accretionary prism revealed from LWD borehole images and their correlation with seismic profile and core data: Results from NanTroSEIZE Stage 1 expeditions, Geochemisry Geophysics, Geosystems 12, Q0AD15, doi:10.1029/2010GC003365.

Yamada, Y., Yamashita, Y., Yamamoto, Y., 2010. Submarine landslides at subduction margins: Insights from physical models. Tectonophysics 484, 156–167. doi:10.1016/j.tecto.2009.09.007